



An approach to modelling defocusing and keyhole reflectivity in keyhole laser processes

Panagiotis Stavropoulos¹ · Georgios Pastras¹ · Konstantinos Tzimanis¹ · Theodoros Bekiaris¹ · Thanassis Souflas¹

Received: 5 February 2024 / Accepted: 10 July 2024 / Published online: 30 July 2024
© The Author(s) 2024

Abstract

Keyhole laser-based processes have been adopted widely due to the high-quality welds and cuts that they produce and the accurately controlled dimensions of the end part. Fast-running simulation tools are required in order to estimate the dependence of process outputs, efficiency, and stability on the process variables. This work presents a fast-running simulation tool for keyhole laser-based processes with inert or no assisting gas that takes into account the effect of laser beam defocusing and the alteration of the effective reflectivity of the material due to the keyhole cavity. The model is built upgrading a successful model for the thermal phenomena based on finite differences and the enthalpy method. The presented model is compared to experimental results for the laser cutting process with both CO₂ and fiber laser sources and inert assisting gas. The model accurately predicts cutting depth and kerf, heat-affected zone width, and the dependence of the cutting depth on the position of the focal plane. The model manages to achieve reduced computational time enabling its utilization in process digital twins.

Keywords Laser-based processes · Keyhole · Laser cutting · Laser beam defocusing · Effective reflectivity of keyhole · Digital twin

1 Introduction

Laser-based processes have found applications in an increasing number of industries over the years, since they provide high flexibility, as it regards the shape of parts that can be created and the variety of materials that can be processed, based on their ability to produce structures and cut materials that cannot be processed with conventional machining methods. They rely on laser attributes such as narrow heat-affected zone, narrow kerf, shallow angle hole, large aspect ratio holes, very small diameter holes, odd shapes, cavities and slots, machining of inaccessible locations, non-contact machining (no tool force), machining of soft, and very hard materials and cutting very brittle and very ductile materials [1]. The output of laser-based processes can be used either directly without post-processing or after re-working specific areas in order to achieve the desired tolerances. In addition to the advantages of high speed, tight tolerances, and

good surface quality, the laser is ideal for interfacing with robots in computer-aided design/computer-aided manufacturing (CAD/CAM) systems, allowing the efficient and cost-effective manufacturing of parts for specific applications [2, 3].

Laser-based processes are divided into two broad classes, based on the heating mode: keyhole-mode and conduction-mode processes. Their main difference is identified on the laser beam power density. In the conduction-mode processes, the power density causes the metal to melt and the weld penetration is achieved by heat conduction across the height of the part from the surface. On the other hand, during keyhole processes, the power density is high enough to cause vaporization of material, which in turn leads to expanding gases that push outwards. This condition creates a keyhole from the surface across the height, moving the material. By moving the laser beam across the surface, the keyhole follows the same path, creating a deep and narrow tunnel. Some of the major factors in cut kerf formation are the temperature distribution on the melt surface, the thickness of the molten layer, and the temperature gradients. The melt surface motion and thereby the melt material ejection are driven by pressure differences which consist of two contributions: one from the cutting gas jet and one from the pressure of evaporated or decomposed material.

✉ Panagiotis Stavropoulos
pstavr@lms.mech.upatras.gr

¹ Laboratory for Manufacturing Systems and Automation, Department of Mechanical Engineering and Aeronautics, University of Patras, Rio, Patras 26504, Greece

Representatives of keyhole laser-based processes are keyhole welding, drilling, and cutting, while additive manufacturing (AM) processes and conduction welding belong to the class of conduction-mode processes. Key parameters for the decision-making are the surface quality after material removal, the melt pool dimensions, and the capabilities of the machine with respect to the thermo-physical properties of the material [4, 5]. This work focuses on the modelling of keyhole laser processes, building on a successful modelling approach for conduction laser processes [6].

The laser spot diameter, the laser medium, which determines the laser wavelength, the maximum power and pulsing mode, either continuous or pulsed, and the pulsing frequency in the latter case are used to characterize the capabilities of a laser machine on performing processes on specific materials [1, 7]. These capabilities are also affected by material properties, such as reflectivity at the laser wavelength. The number of laser beams and their orientation (co-axial or off-axis), the optical chamber (lens, mirrors, etc.), and the distance from the workpiece are factors that affect directly the performance of the laser-based process, since they may affect the position of the focal plane, as well as the footprint of the laser beams on the workpiece. In laser welding and cutting, the position of the focal plane is a parameter that determines the laser spot size on the surface, as depicted in Fig. 1.

The formation of a keyhole alters the distance of the focal plane to the plane where material-laser interaction takes place [8]. As a result, the in-falling intensity, which is the most important quantity that determines the process performance, depends on the keyhole geometry. It follows that the defocusing of the laser beam has to be taken into account.

A technical difficulty that appears in the determination of the in-falling heat fluxes to the simulation grid elements originates from the motion of the laser head relative to the workpiece. As a result of this motion, the heat fluxes are time-dependent. If their calculation is performed numerically, it will significantly add to the computational complexity of the algorithm, since it has to be repeated at every time step of the algorithm. In this work, we present an analytic method

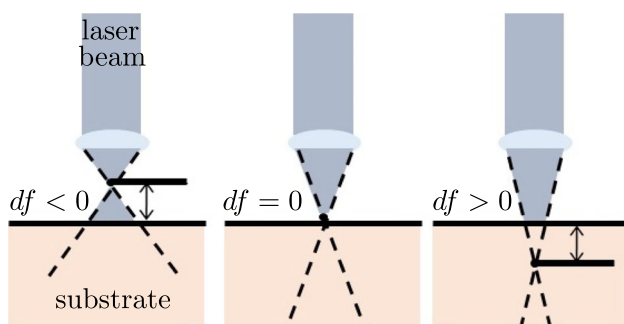


Fig. 1 Laser beam defocusing

for the calculation of these fluxes, which is based on Owen's T function, that bypasses these difficulties.

Another important effect that appears when keyholes are formed is the variation of the apparent material reflectivity due to the keyhole cavity geometry. In principle, the determination of the heat flux from the incident laser beam requires the solution of the electromagnetic wave equation with appropriate boundary conditions at the keyhole surface. Such an approach is computationally demanding and complicates significantly the process simulation. In this work, we take advantage of the fact that typically the dimensions of the keyhole are one to three orders of magnitude larger than the laser wavelength. As a result, a geometric approach for light propagation and reflection can be considered a good approximation. In this approach, the reduction of the apparent reflectivity due to the formation of the keyhole is a consequence of the fact that a light ray may get reflected by the keyhole walls more than once until it permanently leaves the keyhole cavity. The multiple reflections on the side walls of the keyhole contribute to the heat input in all respective areas.

Having identified the significance of keyhole formation in laser-based processes, as well as the industrial need for fast-running models that lead the decision-making as it regards the set of process parameters that can be used for different materials and laser characteristics, this work provides a fast-running model for laser cutting process that tackles the consequences of keyhole in the modelling without integrating computational fluid dynamics (CFD) on the model. This work builds on a model that has been recently introduced by P. Stavropoulos et al. [6] for the thermo-physical phenomena in conduction laser processes. The latter addresses the challenges of these laser-based processes and has been validated in the Laser-Based Powder Bed Fusion (PBF-LB/M) case, where no keyhole phenomena are expected.

In this work, the developed model is validated through its comparison to experimental works on the laser cutting process with continuous, both CO_2 and fiber lasers. The model predicts key performance indicators (KPIs) of the process such as the kerf angle, the achieved width, and the depth of cut, based on the given laser beam characteristics, the process parameters, and the material properties. The developed model is a fast-running tool that is focused mainly in the processes where inert or no assisting gas is used.

While the fast performance of the developed model will be quantified in what follows, we would like to state what we mean when we use the term "fast" for a simulation tool. As such, we describe a simulation tool that can complete a task in time of the order of minutes, and thus, it can be a useful tool for an engineer in order to take decisions regarding process parameters. On the contrary, simulation tools that complete a task in time of order of days may have great academic value and probably improved accuracy; however, they are not

particularly useful for the engineer, and are not characterized as “fast.”

Typical cases of keyhole processes, where the developed model applies, include nitrogen-assisted laser cutting and keyhole laser welding, where no assisting gas is used. In the first case, inert gas contributes to improve surface quality without significantly affecting the kerf geometry. In the second case, the primary use of the assisting gas is the prevention of oxidation. As a result, much lower assisting gas flow rates are used.

1.1 Critical phenomena in keyhole processes

In the literature, most approaches for the modelling of laser-based processes include both thermo-physical and fluid dynamics phenomena, resulting in large computational times. More recently, fast-running simulation tools for conduction laser-based processes have been developed [6]. A key feature of these tools is the consideration of only the most important physical phenomena that affect the process performance. The main goal of this work is the extension of this kind of fast-running simulation tool in the case of keyhole laser-based processes. It follows that it is necessary to identify any additional critical physical phenomena that significantly affect the performance of keyhole laser processes, but not that of conduction-mode ones. It is further required to specify whether these can be included in a fast-running simulation tool and determine the widest class of keyhole laser processes that can be simulated fast, i.e., those that are not strongly affected by difficult-to-simulate phenomena.

For this purpose, in this section, various literature sources have been examined in order to guide the assumptions that should be made in the modelling approach. The determination of the key physical phenomena and their significance is of great importance. For the modelling of laser cutting, it is important to detect the significance of the assisting gas on the melt pool dimensions and the effectiveness of the process, as well as to quantify this effect [9]. On the following paragraphs, the key phenomena for the modelling approach are extracted alongside with an insight about the computational time and the desired level of accuracy from the various models based on the application [10].

Although there are many complex phenomena that occur during the laser-based processes, fast-running models are required for fast responses and decision-making [11, 12]. Models that run in the magnitude of hours should be improved. As an example, in a simulation approach where the thermal, electromagnetic, and fluid flow phenomena are taken into account for the simulation of a time period of 10msec in a laser welding process [13], the computational time was around 16h in a work station dedicated for simulations. In another approach that takes into account both

the melt pool flow dynamics and the thermal phenomena, the simulation of 1msec takes around 14h [14]. On the other hand, the computational time can be reduced significantly when the modelling relies only on the thermal phenomena. In a simulation of the PBF-LB/M that relies only on the thermal phenomena, the simulation time is around 30min, for 10msec of process [6]. In all three works mentioned above, the computational power of the used workstations was similar, as is the one that is used in this work.

The performance of the model is also affected by the good understanding of the process mechanism and its sensitivity on various process parameters. It has been shown that the laser wavelength is a very important parameter for the laser-based processes [15, 16]. The temperature field at the area of interaction between the workpiece material and the laser beam depends strongly on the laser source. This is due to the fact that the reflectivity of the material depends strongly on the laser wavelength.

The apparent reflectivity is affected by the existence of the keyhole. Deep keyholes are surface features which almost totally absorb the in-falling power of the laser beam. For example, keyhole laser welding can result in excellent welds with great depth and great depth-to-width ratio [15]. The formation of keyholes has been studied extensively, since it affects directly the process mechanisms, performance, and efficiency, as well as the surface quality of the cut. Keyholes are formed when a focused laser beam strikes the workpiece and the material vaporizes almost without melting due to the extremely high-power density [17, 18]. The geometry of a keyhole is depicted in Fig. 2.

The keyhole conical geometry deforms the area where the laser beam interacts with the substrate, affecting its reflectivity. In a geometrical optics approach, Monte Carlo analysis has been used to simulate the multiple reflections in the keyhole area that generate an additional incoming heat current

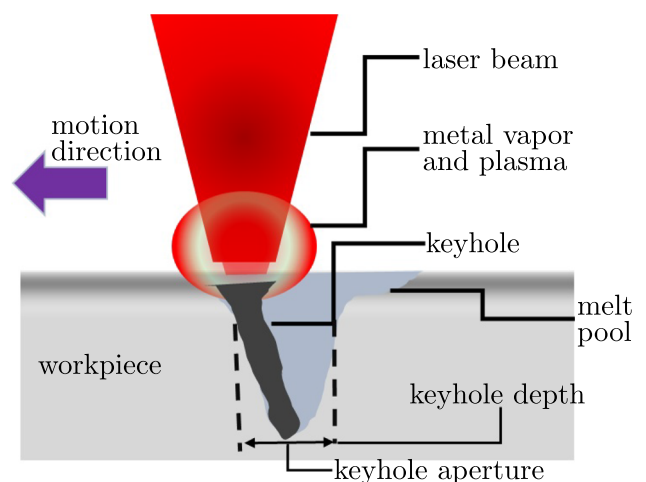


Fig. 2 Keyhole critical dimensions

on the keyhole walls [15]. This kind of phenomena should be taken into account in the simulation of keyhole laser processes.

In the literature, the phenomena are divided into those that are related to the penetration mechanisms (driven by the recoil pressure, emphasized by the beam trapping effect) and those that remove material and can be characterized as opening mechanisms (driven by the melt flow, helped by backward reflections) [19]. The effect of the laser head speed on the governing mechanism has been also investigated [6, 19].

Lower scanning speed favors the penetration mechanisms and the generated keyhole is narrow with consistent geometrical characteristics [19]. On the contrary, higher speed favors the opening mechanism and the produced keyholes look shallow and elongated. In keyhole laser processes, the keyhole aperture affects the process stability. The stability is determined by a critical quantity which is the aspect ratio between the keyhole depth and the focal spot [15]. Therefore, it can be concluded that speed and power, as well as the surface quality (polished, shiny, blurred, etc.) and the reflectivity of the substrate material, affect the dimensions of the keyhole (both width and depth).

The keyhole depth affects the distance between the laser head and the surface of interaction of the laser beam with the material. Laser-based processes, such as cutting and welding, are very sensitive on the distance between the focal plane and the substrate due to laser beam defocusing [20]. Laser beam defocusing has been studied extensively since it is correlated to the performance and the efficiency of the keyhole laser processes. In some works, the laser beam has been defocused on purpose in order to modify the laser spot size in an effort to control the geometry of the weld pool as well as to optimize and stabilize the laser welding process [10]. Apart from the controlled geometry, the effect of defocusing on the mechanical properties of the part and finally on its strength has been studied [21, 22].

The controlled focal intensity of the laser beam affects the amount of energy that is dissipated in the laser spot, creating a more uniform temperature field and then less internal stresses [23–25]. As visualized in Fig. 1, the footprint of the laser beam, the angle between the laser beam, and the substrate surface are subjected to significant changes due to the defocusing [9].

It has been experimentally validated that there is a critical focal plane position where the optimum performance of the laser beam can be achieved [26]. Focusing above this position leads to a very stable melt pool, while below this value, deep keyholes are formed. The optimal focal plane position depends on the workpiece material [26]. On the contrary, it is independent to the laser power [27]. Mei et al. have developed a model for keyhole processes that aims to quantify the effect of the laser parameters on the keyhole formation, simultane-

ously identifying the exact value of the critical focal plane position [15]. Considering the latter, it was found that when the focal plane lies into the workpiece, the penetration depth increases by lowering the focal plane up to an optimum value. It was concluded that the optimal focal plane position lies at about one-third of the full penetration depth, below the workpiece surface, in both laser cutting and keyhole laser welding processes.

Another important process feature in the case of laser cutting is the assisting gas. Inert gas affects only the quality of the surface and not the geometrical features of the process. On the contrary, when active assisting gas is used, the relevance of the gas in the laser cutting process is highlighted, insisting that the maximum cutting rate and the cutting kerf are affected even more significantly by the force/pressure/velocity exerted by the assisting gas than they are affected by the laser power [1, 28–32].

The key conclusions from the effect of inert and active gas in keyhole laser-based processes are summarized below. However, in the keyhole laser welding process, no high-pressure, active assisting gas is used, since the melt material should be used for the bonding and not be removed.

- Inert assisting gas is used to improve the quality of the cut zone. Edge quality is affected by the type of assisting gas (compressed air, inert gas) [33].
- Surface quality is improved by reducing the cutting speed, increasing the laser power, and increasing the pressure of the assisting inert gas [34].
- The laser power value and the thickness of the material determine the most suitable gas [33].
- The kerf size increases considerably as the laser power increases and the cutting speed decreases.
- Summing up, active assisting gas significantly alters the keyhole geometry, whereas inert assisting gas does not [33].

Summing up, we conclude that a fast-running model for the simulation of keyhole laser processes should definitely include laser beam defocusing and a model for the increase of absorptivity due to the keyhole formation. Such an approach cannot be realized for processes where active gas is used, since there fluid dynamics and chemical phenomena play a significant role.

The rest of the document is structured as follows: In Section 2, the modelling approach is presented, focusing on the analytic calculation of heat fluxes, the modelling of laser beam defocusing, and the treatment of multiple reflections of the laser beam. Section 3 is dedicated to the model validation and the provision of model outputs. The manuscript ends with the conclusion and discussion sections, namely Sections 5 and 4, where the ongoing and future work are introduced.

2 Modelling approach

The goal of this work is the development of a fast-running simulation tool for keyhole laser processes with a moving laser head. According to the literature review presented in Section 1.1, the inclusion of fluid dynamics severely adds to the computational complexity and results in large computational times, which are not appropriate for decision-making tools. For this reason, our modelling approach is based on the enthalpy method-based finite-differences approach introduced by Stavropoulos et al. [6], which focuses on the fast simulation of the thermal phenomena during the process.

However, this approach has been developed for the modelling of additive manufacturing processes, which belong to the class of conduction laser processes. For this reason, it neglects the phenomena of laser beam defocusing and the alteration of the workpiece reflectivity due to the geometry of the keyhole, which are important and cannot be neglected in keyhole laser processes, as we have discussed in Section 1.1. Notice that an enthalpy method-based finite-differences model has been used in the past in order to simulate a keyhole laser process, namely keyhole laser welding [8]. However, this was a more academic approach, where laser defocusing was taken into account; however, the alteration of reflectivity due to the cavity was not, but most importantly, the process was considered a stationary laser head process.

The goal of this work is the inclusion of laser defocusing and reflectivity alteration due to the formation of the keyhole to the enthalpy method-based finite-differences model [6], but in a way that is not going to introduce significant computational complexity to the algorithm. A technical difficulty that is present is the fact that the in-falling energy flux by the laser beam is time-dependent, since the laser head moves and is distributed in a complicated way to the lattice cells, due to the geometry of the keyhole and laser defocusing. This problem does not appear in previous approaches, since in conduction laser processes, defocusing is neglected and the energy fluxes can be expressed analytically in terms of the error function [6], whereas in cases where the laser head is considered stationary, the fluxes can be calculated beforehand for all cells of the lattice [8]. In the cases we are interested to simulate, a straightforward method to resolve this issue would require a numerical integration at each time instant in order to specify the in-falling energy flux in each lattice cell. This would lead to a significant increase of calculation times. For this reason, we insisted on the analytical calculation of the energy fluxes in terms on special functions and we managed to express the fluxes in terms of Owen's T function, avoiding the additional computational complexity that would be induced by the numerical integrations.

Finally, we would like to underline that this modelling approach is not appropriate when the thermophysical phe-

nomena are significantly disturbed by chemical phenomena, namely when active assisting gases are used, as discussed in Section 1.1. The model that we developed is appropriate for keyhole laser processes with inert or no assisting gas. The modelling of keyhole laser processes with active assisting gas is beyond the scope of this work.

2.1 The enthalpy method-based finite-differences model

The modelling of the thermophysical phenomena that take place during laser-based processes is very complicated even without the inclusion of the extra difficulties introduced by keyhole formation. The most significant reason for that is the fact that several phase transitions take place. These phase transitions set the thermodynamic equations that govern the diffusion of heat to be non-linear, even if the thermophysical properties of the workpiece (specific heat, thermal conductivity, mass density) are considered constant.

The naive approach to solve this kind of problem is the division of the workpiece to dynamical regions, one for each phase. Then, the heat equation must be solved in each region, and the boundaries should evolve by the related Stefan conditions. This approach is computationally complicated and slow. On the contrary, the problem can be simplified by the introduction of an auxiliary field, that of the enthalpy density. Then, the temperature-dependence of the thermophysical properties of the workpiece material, as well as the latent heat of the phase transitions, can be absorbed into the relation between the temperature and the enthalpy density. This relation may be a complicated non-linear relation, yet it is algebraic. Via the introduction of this auxiliary field, the problem may be split into two parts at each time step, the determination of the heat currents by the temperature field, i.e.,

$$\vec{J} = -k\vec{\nabla}T, \quad (1)$$

and thus the variation of the enthalpy density field, namely

$$\frac{\partial H}{\partial t} = -\vec{\nabla} \cdot \vec{J} = k\vec{\nabla}^2 T. \quad (2)$$

This part of the time step is differential, yet it is linear. The second step is the determination of the new temperature field by the new enthalpy density field, i.e.,

$$T = T(H). \quad (3)$$

This step is non-linear, yet it is algebraic. At this step, the phase of each lattice cell should be updated via the comparison of its enthalpy density to the critical values of enthalpy density that separate the phases.

The virtue of the method is the fact that the combination of the two parts of each time step does not alter the nature of

the problem, which remains a first-order differential equation with respect to time. Therefore, the enthalpy method leads to a fast-running time-stepping algorithm that can be integrated step by step via a simple finite-differences formulation of the problem. The reader is encouraged to consult the original paper [6] for more details on the algorithm and how it has been already implemented for other non-keyhole laser processes.

2.2 Laser beam defocusing

The original model [6] does not take into account laser defocusing. Therefore, the laser beam below the workpiece surface, or more accurately below the focal plane, is mistakenly assumed to be more focused and intense than it actually is. As a direct result, the original model is expected to overestimate the achieved depth of the keyhole and at the same time to underestimate the kerf of the keyhole, especially at large depths.

In the following, we develop the analytic model of the heat fluxes induced by the in-falling laser beam on the workpiece surface at the presence of a keyhole. We assume a Gaussian laser intensity profile at the focal plane.

$$I(r) = \frac{2P}{\pi r_0^2} e^{-2\frac{r^2}{r_0^2}}, \tag{4}$$

where P is the laser beam power. The quantity r_0 is usually called the laser beam radius. About 86.5% of the total energy of the laser beam is radiated within the $r < r_0$ disk.

Let us consider another plane parallel to the focal one. Due to defocusing, the laser intensity is altered in a uniform way,

$$I(r, z) = \frac{2P}{\pi r_b^2(z)} e^{-2\frac{r^2}{r_b^2(z)}}, \tag{5}$$

where z is the coordinate along the direction of the laser beam axis. The function $r_b(z)$, i.e., the effective spot size, is given by the usual hourglass function, namely,

$$r_b(z) = r_0 \sqrt{1 + \left(M^2 \frac{\lambda (z - z_0)}{\pi r_0^2} \right)^2}, \tag{6}$$

where z_0 is the value of the coordinate z at the focal plane, M^2 is the so-called beam quality parameter, and λ is the laser wavelength. The shape of the laser beam is depicted in Fig. 3.

It follows that the laser intensity reduces as we move further from the focal plane. Notice that the deformation of the intensity profile is completely homogeneous; for example,

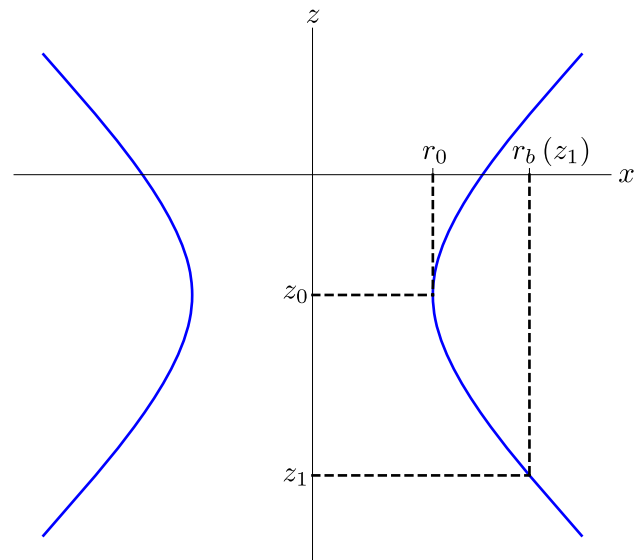


Fig. 3 Laser defocusing

at any plane that is parallel to the focal one, 86.5% of the energy is radiated through the $r < r_b(z)$ disk.

2.3 Reflectivity and angle of incidence

Electromagnetic waves upon incidence on the surface of a metallic object set the free electrons of the metal in motion generating currents and thus heat losses due to the Joule phenomenon. As a result, electromagnetic waves are only partially reflected on metallic surfaces. The rest of the energy is transformed into heat in the body of the metal. The latter is formed mainly close to the metallic surface as the electric field presents an exponential decrease with the depth inside the metal, due to the shielding by the induced electric currents.

The reflection and absorption coefficients depend on the angle of incidence of the electromagnetic wave and the angle between the polarization vector of the incident electromagnetic wave and the metallic surface. Specifically, the reflection coefficients for the s-polarized and the p-polarized wave are given by

$$R_p = \frac{\left(n - \frac{1}{\cos \theta} \right)^2 + k^2}{\left(n + \frac{1}{\cos \theta} \right)^2 + k^2}, \tag{7}$$

$$R_s = \frac{(n - \cos \theta)^2 + k^2}{(n + \cos \theta)^2 + k^2}, \tag{8}$$

where n is the refractive index and k is the extinction coefficient, which depends on the electric conductivity of the metal. In general, both n and k depend on the wavelength of the incident electromagnetic wave. Finally, θ is the angle

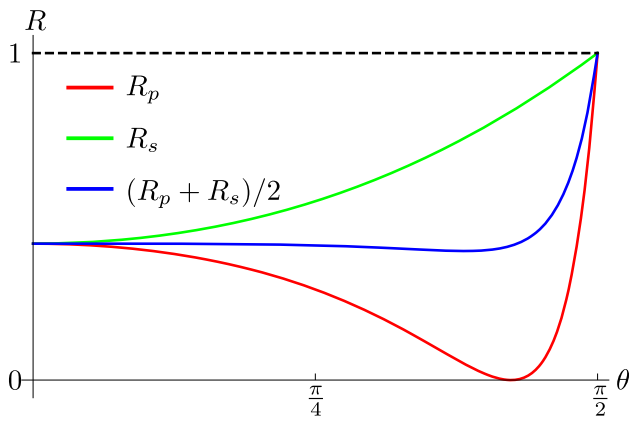


Fig. 4 Reflectivity as function of the angle of incidence

between the direction of incidence and the perpendicular to the metallic surface. In the rest of this paper, the polarization is considered arbitrary, implying the reflection index is equal to

$$R = \frac{R_p + R_s}{2}. \tag{9}$$

The dependence of the reflective index on the angle of incidence for a typical metal (iron) is depicted in Fig. 4.

We would like to point out that the polarization selection can give rise to interesting options for the process. For example, in processes with moving laser heads (i.e., laser welding, laser cutting), the selection of a polarization that is parallel or perpendicular to the laser head motion can give rise to a variation of the absorption coefficients, with obvious consequences for the energy efficiency and the general performance of the process.

2.4 The heat currents

We model the workpiece in a uniform rectangular lattice. Let $2\delta x$, $2\delta y$ and $2\delta z$ be the dimensions of the lattice cells. Let us also assume that the focal plane is the $z = 0$ plane and that the lattice extends from the focal plane and below. Finally, for simplicity of the considerations in this section, we assume that the laser beam axis coincides with the z -axis ($x = y = 0$), as shown in Fig. 5.

It is not difficult to calculate the in-going heat current due to the laser beam on any lattice element on the surface of the workpiece. Consider an element which is centered at $x = x_0$ and $y = y_0$. For notational simplicity, we define $x_{\pm} := x_0 \pm \delta x$ and $y_{\pm} = y_0 \pm \delta y$. Then, the heat current that enters this cell is equal to

$$\frac{dQ_0}{dt} = (1 - R) P_0, \tag{10}$$

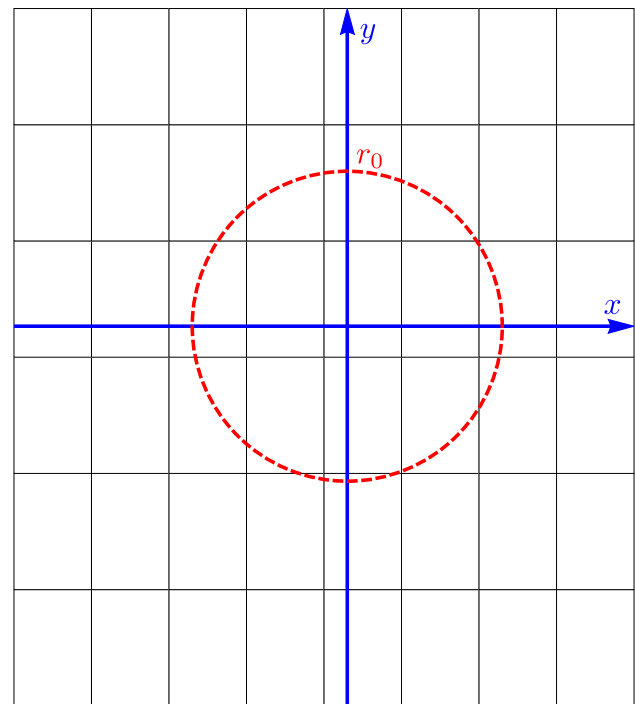


Fig. 5 The lattice cells hit by the laser at the focal plane

where R is the reflectivity and P_0 is the in-falling laser radiant power in this cell. The latter equals

$$\begin{aligned} P_0 &= \int_{x_-}^{x_+} dx \int_{y_-}^{y_+} dy \frac{2P}{\pi r_0^2} e^{-2\frac{r^2}{r_0^2}} \\ &= \frac{P}{4} \left(\operatorname{erf} \frac{\sqrt{2}(x_0 + \delta x)}{r_0} - \operatorname{erf} \frac{\sqrt{2}(x_0 - \delta x)}{r_0} \right) \\ &\quad \times \left(\operatorname{erf} \frac{\sqrt{2}(y_0 + \delta y)}{r_0} - \operatorname{erf} \frac{\sqrt{2}(y_0 - \delta y)}{r_0} \right) \\ &\equiv W_h(r_0; x_0, y_0; \delta x, \delta y), \end{aligned} \tag{11}$$

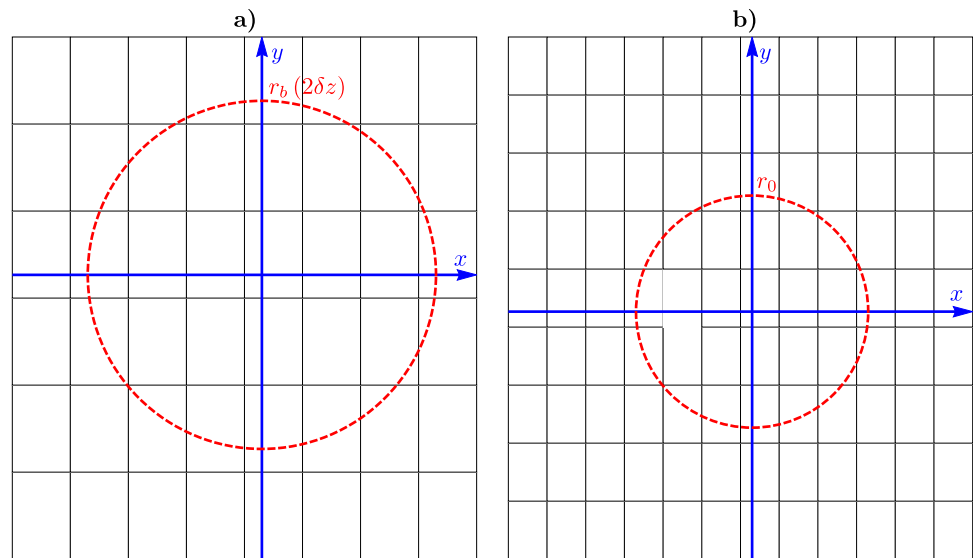
where $\operatorname{erf}(x)$ stands for the error function.

In an obvious manner, if we had considered that the first level of cells of the lattice had been evaporated, and, thus, the laser was heating the second layer of cells, then the laser intensity would have been given by the same exact formula, upon the substitution of r_0 with $r_b(2\delta z)$, and thus,

$$P_1 = W_h(r_b(2\delta z); x_0, y_0; \delta x, \delta y). \tag{12}$$

Defocusing implies that intensity decreases with depth, i.e., $W_h(r_b(2\delta z); x_0, y_0; \delta x, \delta y) < W_h(r_0; x_0, y_0; \delta x, \delta y)$. We may conceive this fact in two different, but equivalent, ways. The obvious one is to consider that the laser beam radius has expanded relatively to that at the focal plane, leading to a suppression of the arguments of the error functions

Fig. 6 The two equivalent descriptions of the lattice cells at some depth being hit by the laser: **a** expanded beam radius and **b** shrunk cells



appearing in formula Eq. 13, thus to a reduction of the laser radiant power and the heat current. Completely equivalently, one could imagine that the laser beam radius has remained the same, but the quantities x_0 , y_0 , δx , and δy have shrunk by a factor $\kappa \equiv \frac{r_0}{r_b(2\delta z)}$, since

$$W_h(r_b(2\delta z); x_0, y_0; \delta x, \delta y) = W_h(r_0; \kappa x_0, \kappa y_0; \kappa \delta x, \kappa \delta y). \tag{13}$$

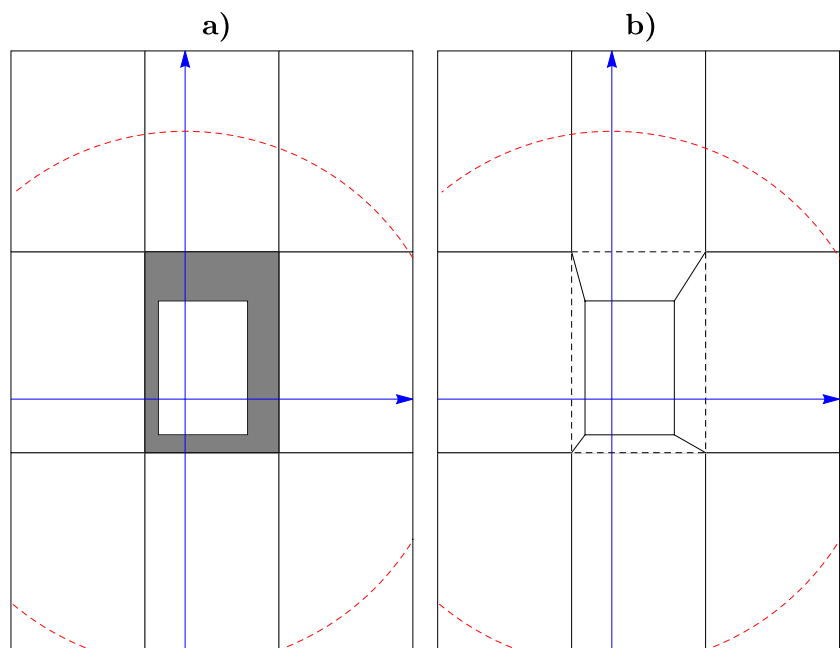
This equivalent point of view is possible, because the defocusing of the laser beam is homogeneous. As a result, the in-falling power on a cell whose top surface lies at a depth $z = 2\delta z$ is actually the power that crossed through the focal

plane, but through a smaller rectangle. This smaller rectangle is the top surface of the cell under consideration homogeneously, shrunk with respect to the center of the laser beam. Therefore, we may visualize the effect of defocusing as a uniform shrinking of the lattice along the x - and y -directions towards the laser beam center $x = y = 0$. These two equivalent points of view of the effect of defocusing are depicted in Fig. 6.

Let us consider only the element of the lattice, that is below the laser beam center. What are the radiant energy currents now? The answer is essentially given by the Fig. 7.

All elements on the top layer receive the same radiant energy currents as in our previous considerations, except for

Fig. 7 One cell of the top layer missing. **a** The energy flux that results in the vertical exposed faces of the lattice. **b** The distribution of energy flux in the exposed lattice cells



the missing evaporated cell. The element below the evaporated cell receives the current which crosses the focal plane through the white rectangle within the gray frame at the left panel of Fig. 7. This fact follows from the discussion above on the two equivalent descriptions of the effect of defocusing on the radiant energy currents. Where the energy current that crosses the focal plane through the gray frame is going? The answer is simple. Due to the form of the laser beam, a part of the radiant energy is falling on the vertically exposed faces of the cells that are neighboring to the evaporated cell. It is simple to understand how these currents are divided between these cells; it is depicted in the right panel of Fig. 7. More importantly, this figure clarifies how to calculate these currents. For example, the radiant energy current that is in-falling to the exposed vertical side of the cell to the left of the evaporated cell is

$$P_v = \int_{\kappa x_+}^{x_+} dx \int_{\frac{y_-}{x_+}}^{\frac{y_+}{x_+}} dy \frac{2P}{\pi r_0^2} e^{-2\frac{r^2}{r_0^2}}. \tag{14}$$

This integral is easier to manipulate in polar coordinates

$$\begin{aligned} P_v &= \int_{\tan^{-1} \frac{y_-}{x_+}}^{\tan^{-1} \frac{y_+}{x_+}} d\varphi \int_{\frac{\kappa x_+}{\cos \varphi}}^{\frac{x_+}{\cos \varphi}} dr r \frac{2P}{\pi r_0^2} e^{-2\frac{r^2}{r_0^2}} \\ &= \frac{P}{2\pi} \int_{\tan^{-1} \frac{y_-}{x_+}}^{\tan^{-1} \frac{y_+}{x_+}} d\varphi \left(e^{-\frac{2\kappa^2 x_+^2}{r_0^2 \cos^2 \varphi}} - e^{-\frac{2x_+^2}{r_0^2 \cos^2 \varphi}} \right). \end{aligned} \tag{15}$$

We perform the change of variable $\tan \varphi = u$, which implies that $(1 + u^2) d\varphi = du$. This allows the writing of the last integral as

$$\begin{aligned} P_v &= \frac{P}{2\pi} \int_{\frac{y_-}{x_+}}^{\frac{y_+}{x_+}} du e^{-\frac{2\kappa^2 x_+^2}{r_0^2} (1+u^2)} \frac{e^{-\frac{2x_+^2}{r_0^2} (1+u^2)}}{1+u^2} \\ &= \frac{P}{2\pi} \int_{\frac{y_-}{x_+}}^{\frac{y_+}{x_+}} du \int_{\frac{2\kappa^2 x_+^2}{r_0^2}}^{\frac{2x_+^2}{r_0^2}} dw e^{-w(1+u^2)} \\ &= \frac{P}{4\sqrt{\pi}} \int_{\frac{2\kappa^2 x_+^2}{r_0^2}}^{\frac{2x_+^2}{r_0^2}} dw \frac{e^{-w}}{\sqrt{w}} \left(\operatorname{erf} \frac{\sqrt{w} y_+}{x_+} - \operatorname{erf} \frac{\sqrt{w} y_-}{x_+} \right). \end{aligned} \tag{16}$$

But

$$\begin{aligned} \int dx \frac{e^{-x}}{\sqrt{x}} \operatorname{erf}(\sqrt{x}y) &= \sqrt{\pi} \left[\operatorname{erf}(\sqrt{x}y) \operatorname{erf} \sqrt{x} \right. \\ &\quad \left. + 1 + 4T\left(\sqrt{2xy}, \frac{1}{y}\right) \right], \end{aligned} \tag{17}$$

where $T(h, b)$ stands for Owen’s T function, which is defined as,

$$T(h, b) := \frac{1}{2\pi} \int_0^b dx \frac{e^{-\frac{1}{2}h^2(1+x^2)}}{1+x^2}. \tag{18}$$

It follows that

$$\begin{aligned} P_v &= \frac{P}{4} \left[\operatorname{erf} \frac{\sqrt{2}(y_0 + \delta y)}{r_0} \operatorname{erf} \frac{\sqrt{2}(x_0 + \delta x)}{r_0} \right. \\ &\quad - \operatorname{erf} \frac{\sqrt{2}(y_0 + \delta y)}{r_b(2\delta z)} \operatorname{erf} \frac{\sqrt{2}(x_0 + \delta x)}{r_b(2\delta z)} \\ &\quad - \operatorname{erf} \frac{\sqrt{2}(y_0 - \delta y)}{r_0} \operatorname{erf} \frac{\sqrt{2}(x_0 + \delta x)}{r_0} \\ &\quad \left. + \operatorname{erf} \frac{\sqrt{2}(y_0 - \delta y)}{r_b(2\delta z)} \operatorname{erf} \frac{\sqrt{2}(x_0 + \delta x)}{r_b(2\delta z)} \right] \\ &\quad + P \left[T\left(\frac{2(y_0 + \delta y)}{r_0}, \frac{x_0 + \delta x}{y_0 + \delta y}\right) \right. \\ &\quad - T\left(\frac{2(y_0 + \delta y)}{r_b(2\delta z)}, \frac{x_0 + \delta x}{y_0 + \delta y}\right) \\ &\quad - T\left(\frac{2(y_0 - \delta y)}{r_0}, \frac{x_0 + \delta x}{y_0 - \delta y}\right) \\ &\quad \left. + T\left(\frac{2(y_0 - \delta y)}{r_b(2\delta z)}, \frac{x_0 + \delta x}{y_0 - \delta y}\right) \right] \\ &\equiv W_v(r_0, r_b(2\delta z); x_0 + \delta x; y_0, \delta y). \end{aligned} \tag{19}$$

It is not difficult to show that the radiant energy currents through the four exposed vertical faces of the cells that are adjacent to the evaporated cell are

$$\begin{aligned} W_{\text{right}} &= W_v(r_0, r_b(2\delta z); x_0 + \delta x; y_0, \delta y) \\ W_{\text{front}} &= W_v(r_0, r_b(2\delta z); y_0 + \delta y; x_0, \delta x) \\ W_{\text{left}} &= W_v(r_0, r_b(2\delta z); -x_0 + \delta x; y_0, \delta y) \\ W_{\text{back}} &= W_v(r_0, r_b(2\delta z); -y_0 + \delta y; x_0, \delta x) \end{aligned} \tag{20}$$

We need to verify that these four terms sum to the difference of the radiant energy currents through the top and bottom faces of the evaporated cell. The algebra is rather tedious. There are four terms from each contribution, sixteen total, which are expressed as the product of two error functions each. It is not difficult to see that these sum to twice the desired quantity. There are also four terms from each contribution, sixteen total, which are expressed as Owen’s T function. These are organized in two sets of eight terms each, one set expressed in terms of r_0 and one set expressed in terms of $r_b(2\delta z)$. In each octuplet, there are four pairs of terms, whose second arguments are inverse of one another.

For example, in the octuplet expressed in terms of r_0 , there are the contributions from the right and front cells that read

$$W_{\text{right1+front1}} = PT \left(\frac{2(y_0 + \delta y)}{r_0}, \frac{x_0 + \delta x}{y_0 + \delta y} \right) + PT \left(\frac{2(x_0 + \delta x)}{r_0}, \frac{y_0 + \delta y}{x_0 + \delta x} \right). \tag{21}$$

Owen’s T function obeys

$$T(h, b) + T\left(bh, \frac{1}{b}\right) = \frac{1}{4} \left(1 - \operatorname{erf} \frac{h}{\sqrt{2}} \operatorname{erf} \frac{bh}{\sqrt{2}} \right). \tag{22}$$

As a result, the above two terms assume the form

$$W_{\text{right1+front1}} = \frac{P}{4} \left(1 - \operatorname{erf} \frac{\sqrt{2}(x_0 + \delta x)}{r_0} \operatorname{erf} \frac{\sqrt{2}(y_0 + \delta y)}{r_0} \right). \tag{23}$$

The constant term is going to cancel with the constant term from the equivalent terms in the octuplet of terms which is the function of $r_b(2\delta z)$. These four terms add up to

$$-\frac{P}{4} \left(\operatorname{erf} \frac{\sqrt{2}(x_0 + \delta x)}{r_0} \operatorname{erf} \frac{\sqrt{2}(y_0 + \delta y)}{r_0} - \operatorname{erf} \frac{\sqrt{2}(x_0 + \delta x)}{r_b(2\delta z)} \operatorname{erf} \frac{\sqrt{2}(y_0 + \delta y)}{r_b(2\delta z)} \right). \tag{24}$$

In an obvious manner, all sixteen terms add up to the opposite of the desired output, and, thus,

$$W_{\text{right}} + W_{\text{front}} + W_{\text{left}} + W_{\text{back}} = W_{\text{top}} - W_{\text{bottom}}, \tag{25}$$

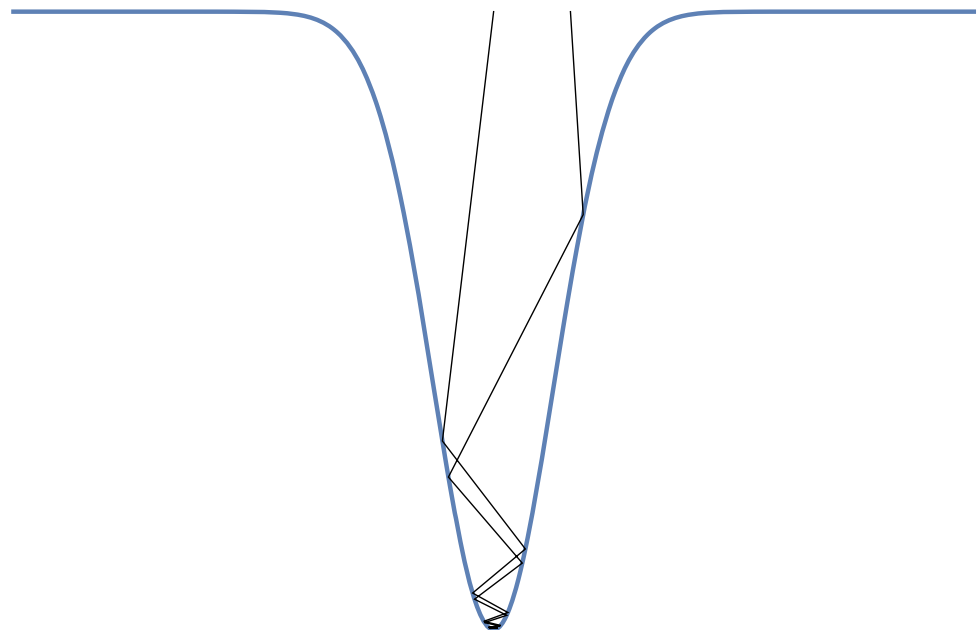
as it should.

2.5 Increase of absorptivity due to the keyhole

An important issue that emerges when a keyhole is formed is the fact that the effective reflectivity of the material is altered due to the cavity of the keyhole. If we neglect this issue, but not laser beam defocusing, we should expect that the model will underestimate the achieved keyhole depth.

In principle, in order to calculate the increase of the absorptivity of the workpiece surface due to the formation of the keyhole, one would need to solve the electromagnetic wave equations with appropriate boundary conditions at the keyhole surface. This direct approach is quite complicated and would significantly increase calculation times. We may follow an alternative approach. Typically, the dimensions of the keyhole are several orders of magnitude larger than the laser wavelength. According to [35], a typical keyhole width varies from 300 to 900 μm , where the minimal width appears at the bottom of the keyhole, whereas the maximal one at the keyhole opening. The wavelength of CO₂ lasers is around to 10.6 μm while for the fiber lasers, this value varies between 0.78 and 2.2 μm [36–40]. It follows that the keyhole dimensions are two to three orders of magnitude larger than the wavelength of the laser beam. This implies that a geometric-optics approach for the propagation and reflection of light in

Fig. 8 The increase of the absorptivity of the workpiece surface due to the keyhole as multiple reflections in a geometric-optics approximation



the keyhole cavity is a good approximation and a useful tool in order to understand the increase of absorptivity due to the existence of the keyhole.

In the language of geometric optics, a laser light ray is reflected several times within the keyhole, before it gets out of the material, as depicted in Fig. 8.

The increase of absorptivity stems directly from this fact. A light ray that gets reflected n times before exiting the keyhole behaves as if it got reflected by a material with an effective reflection coefficient equal to $R_1 R_2 \dots R_n$, where R_i is the reflection coefficient for the i -th reflection. However, neglecting the dependence of R_i on the angle of incidence, i.e., assuming that $R_i \simeq R$, the above effective reflection coefficient is approximately equal to R^n . This is a decreasing function of n , which is expected to increase as the keyhole becomes deeper.

Even in this simple geometric-optics approach, an analytic calculation of the effective reflectivity of the keyhole cavity would require the analytic, continuous, and smooth expression of the keyhole shape, in order to calculate the angles of incidence for all the reflections that a ray undergoes into the cavity and, thus, its path and the effective reflection coefficient. However, the finite-difference approach that is followed in this work enforces the approximation of the workpiece in a rectangular lattice. It follows that no analytic, smooth expression for the shape of the keyhole is available. On the contrary, the keyhole is approximated by a polygonal chain with the accuracy of the orthogonal lattice that has been introduced for the simulation of the process, as shown in Fig. 9.

All keyhole walls appear either horizontal or vertical in our model. Thus, the information necessary to determine the path of a light ray, namely the angles of incidence, has been distorted by the rectangular lattice. However, the geometric-optics approach clearly suggests that reflections on a region where the keyhole surface is almost vertical are more likely to be followed by more reflections. Thus, a reasonable simplifying assumption that follows from the geometric optics

picture is the following: Light rays that fall on horizontal surfaces get reflected out of the cavity, whereas light rays that fall on vertical surfaces get reflected so that they fall once again in cavity walls. We assume that reflected light rays contribute to the overall laser intensity at larger depths of the cavity without altering its spatial distribution. The analytic calculation of the heat currents due to the laser beam in both horizontal and vertical faces of the lattice elements that was presented in Section 2.4 greatly facilitates the calculations regarding the multiple reflections.

The rectangular lattice hides information about the angles of incidence, since all segments of the workpiece surface are approximated as either horizontal or vertical rectangles. This implies that taking into account the dependence of the reflection coefficient on the angle of incidence cannot provide much improvement to the accuracy of the model due to the lack of knowledge of the latter. For this reason, in what follows, the reflection coefficient for all angles is taken to be that of perpendicular incidence. Figure 4 suggests that when an arbitrary polarization is considered, this is a good approximation for a wide range of angles.

3 Validation

3.1 The validation case study

In order to validate the model developed in Section 2, a comparison with experimental results from the literature was performed. The case study geometry is depicted in Fig. 10. The laser source is considered moving along the y -axis, cutting material from a stainless steel AISI 304L plate. The case study comprises of two different laser sources, namely a CO₂ and a fiber laser source. A combination of Neumann and Dirichlet boundary conditions is selected on the edges of the grid along the width and length directions while Neumann conditions are applied at the top and bottom of the grid. The width and the length of the simulated area are

Fig. 9 The approximation of the shape of the keyhole in the rectangular lattice

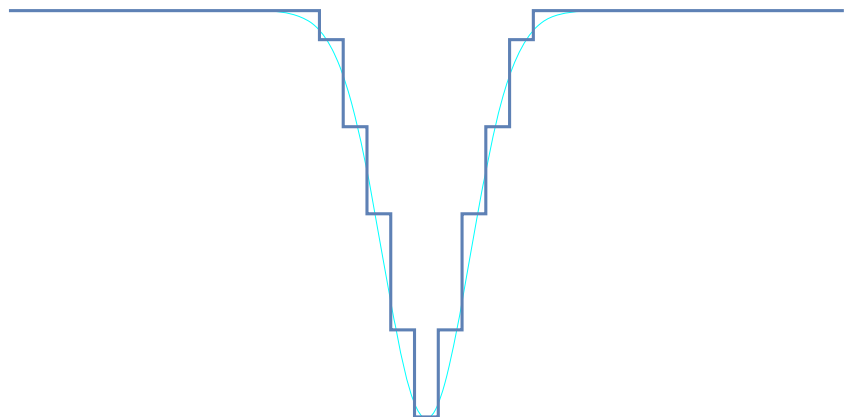
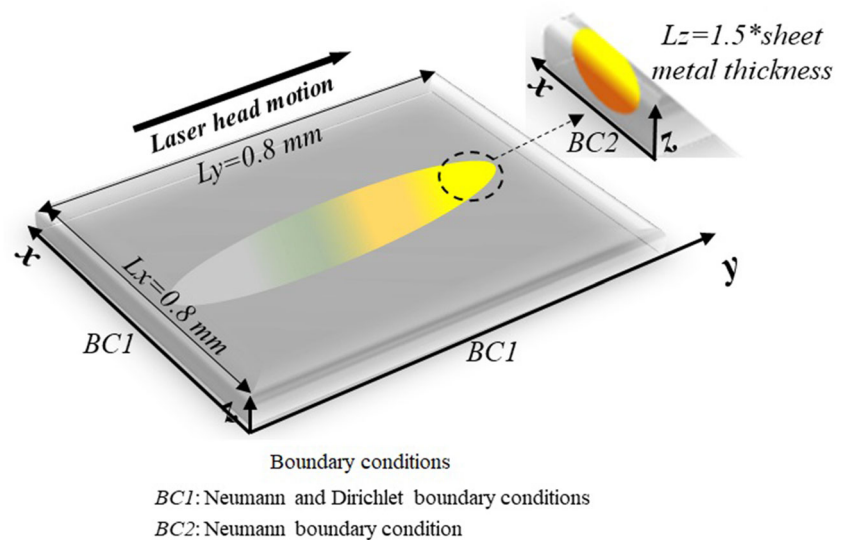


Fig. 10 The geometry of the case study, as well as the boundary conditions applied



0.8 mm × 0.8 mm, respectively, while the simulated sheet thickness is increased by 10% compared to the experimental data, in order to capture the maximum cutting depth without disturbing the bottom boundary conditions significantly.

Table 1 Thermophysical properties of SS304 [41]

Parameter	Symbol	Value
Thermal conductivity at solid phase	k_s	$10.33 \frac{W}{m \cdot K} + (15.4 \times 10^{-3} \frac{W}{m \cdot K^2}) T - (7 \times 10^{-6} \frac{W}{m \cdot K^3}) T^2$
Thermal conductivity at liquid phase	k_l	$6.6 \frac{W}{m \cdot K} + (1.214 \times 10^{-2} \frac{W}{m \cdot K^2}) T$
Specific heat at solid phase	c_{ps}	$443 \frac{J}{kg \cdot K} + (0.2 \frac{J}{kg \cdot K^2}) T - (8 \times 10^{-5} \frac{J}{kg \cdot K^3}) T^2$
Specific heat at liquid phase	c_{pl}	$800 \frac{J}{kg \cdot K}$
Mass density at solid phase	ρ_s	$8169.298 \frac{kg}{m^3} - (0.501 \frac{kg}{m^3 \cdot K}) T$
Mass density at liquid phase	ρ_l	$8198.48 \frac{kg}{m^3} - (0.8 \frac{kg}{m^3 \cdot K}) T$
Latent heat of fusion	L_m	$2.9 \times 10^5 \frac{J}{kg}$
Latent heat of evaporation	L_e	$7.7 \times 10^6 \frac{J}{kg}$
Melting temperature	T_m	1673 K
Evaporation	T_e	3073 K

The actual sheet metal thickness varies between 4 and 10 mm. The simulated width and length have been chosen so that the simulated portion of the actual sheet metal is large enough so that the temperature field on the edges of the simulated region remains approximately at the initial (room) temperature during the process. This ensures that the simulation results are insensitive to the combination of Dirichlet and Neumann conditions applied in these boundaries. The initial temperature is set to 300 K. The selected grid dimensions alongside with the modelling assumptions that have been presented in Section 3 enable the development of a fast-running simulation tool that can provide insights about the effect of process parameters on the process KPIs.

There are some criteria that should be satisfied by the lattice cell dimensions and the time step so that the finite-differences formulation of the differential problem converges to the actual solution of the continuous problem and it does not enter into an oscillatory region. Let δx , δy , and δz be the

Table 2 Laser parameters and optical properties of SS304 for CO₂ and fiber laser

Parameter	Symbol	Value	
		Fiber	CO ₂
Used output power	P	3 kW	3 kW
Wavelength	λ	1.0 μm	10.6 μm
Beam quality factor	M^2	6.2	1.6
Focal radius	r_0	50 μm	85 μm
Focal length	f	254 mm	190 mm
Cutting speed	v	0.5–45 $\frac{m}{min}$	0.5–25 $\frac{m}{min}$
Reflectivity solid	R_s	0.69	0.90
Reflectivity liquid	R_l	0.56	0.86

dimensions of the lattice cells and δt the time step. Then, the convergence criteria read

$$\delta t < \frac{\delta x^2}{2\alpha}, \quad \delta t < \frac{\delta y^2}{2\alpha}, \quad \delta t < \frac{\delta z^2}{2\alpha}, \quad (26)$$

where α is the thermal diffusivity of the workpiece material. Improving the convergence requires reducing the time step, thus increasing the computational time. This should be done until the solution becomes insensitive of further decrease of the time step. Further decrease of the time step does not

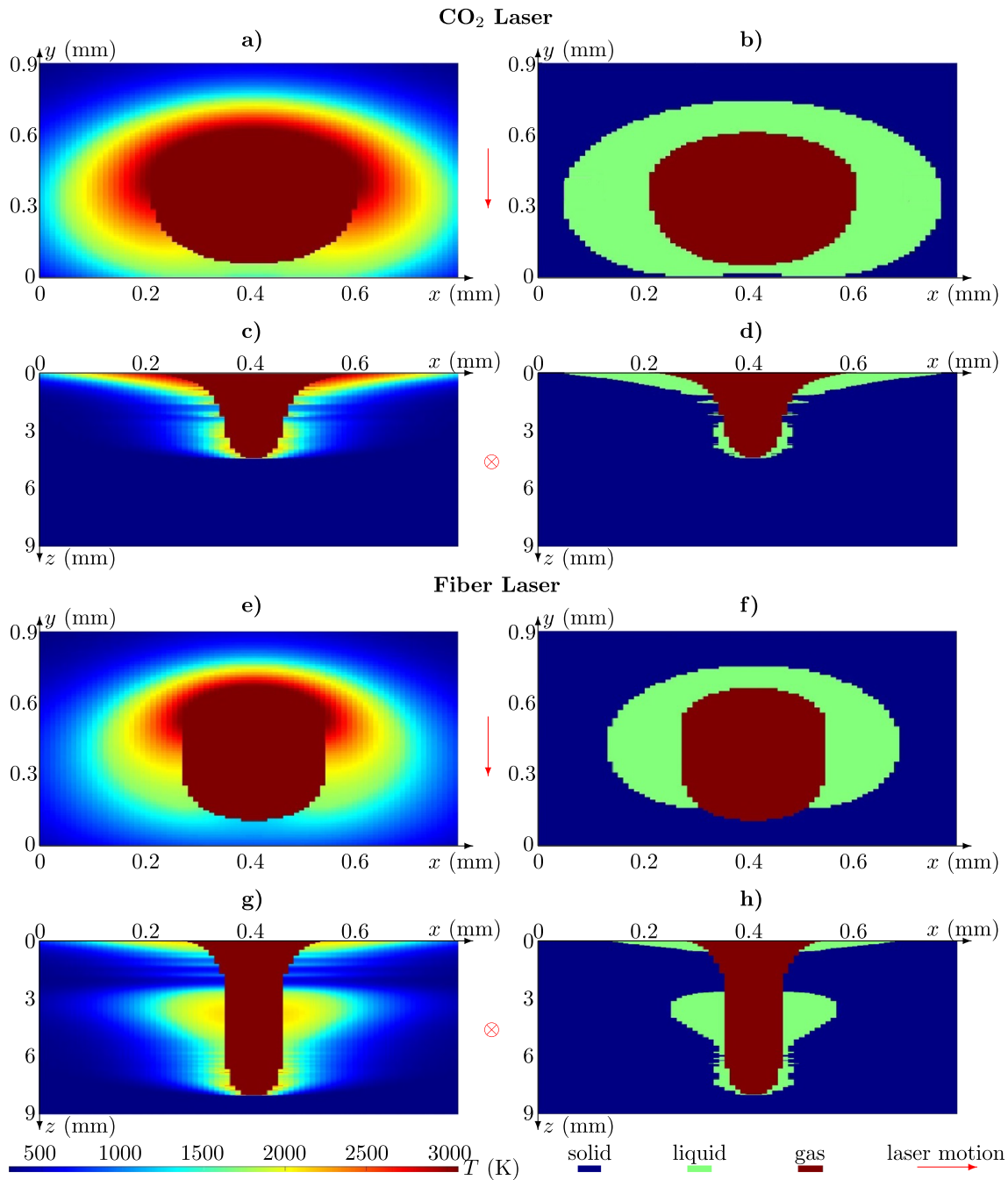


Fig. 11 Indicative temperature (a, c, e, and g) and phase (b, d, f, and h) distributions on the workpiece for CO₂ (a, b, c, and d) and fiber (e, f, g, and h) laser sources on the top horizontal workpiece surface (a, b, e, and f) and the vertical plane that is perpendicular to the laser head motion (c, d, g, and h). The distance of the vertical planes from the laser

head is equal to 4/5 of the distance that the latter has travelled during the simulation, so that the keyhole is fully deployed and the phase distribution has been stabilized considering a stable process with steady-state conditions. Therefore, in these sections, the critical kerf dimensions can be obtained

improve the results and increases the computational time. The analysis resulted in an optimal cell size of $10 \mu\text{m} \times 10 \mu\text{m} \times 16 \mu\text{m}$ and time step of $1 \mu\text{sec}$. Of course, selecting larger values for the cell dimensions appears to facilitate the selection of a larger time step, satisfying at the same time the convergence criteria. However, the dimensions of the cells are bound to physical constraints. For example, the δx and δy should not become larger than the laser spot size in order to capture correctly the in-falling energy flux.

In order to validate the model, the study of S. Stelzer et al. with experimental results was selected [16]. In this study, two different laser sources are examined at cutting stainless steel 304 (SS304). Then, the achieved kerf width at maximum acceptable cutting speed for achieving the required cutting depth was measured. The cases regarded metal sheet thickness varying between 4 and 10 mm. The studied cases are all single tracks.

The developed simulation tool receives temperature-dependent thermophysical and optical properties of SS304 for both its liquid and solid phase as input. A cubic polynomial approximation for these properties was used. The coefficients for the cubic polynomials of the thermophysical properties have been provided from the work of J. Juan et al. on the thermophysical properties of several materials [41] and are summarized in Table 1. The optical properties, namely the reflectivity at the wavelengths of both laser sources are provided by the study of J. Xie et al. [42] and are summarized together with the laser beam parameters in Table 2.

3.2 Keyhole dimensions

A simulation tool was developed based on the model described in Section 2. The tool was built with the use of the language C. The output of the model is the temperature field at any desired time instance, as well as the distribution of phases in the workpiece. The kerf width and the achieved cutting depth from the simulations are extracted by measuring the related dimensions from a phase plot. Indicative outputs of the model are depicted in Fig. 11.

These outputs indicate that there is a distinctive difference at the kerf width between the CO₂ and fiber laser sources. This is due to the larger spot size in the case of CO₂ laser. In addition, the lower reflectivity in the case of fiber laser is the main reason for the greater achieved depth. It is worth mentioning that the area of liquid material that is located in the middle of the cutting depth is caused by the defocusing effect at increased depths. The fiber laser has a higher beam quality factor compared to the CO₂; thus, the defocusing effect is more detrimental in that case.

In order to better understand the influence of the defocusing and multiple reflections provisions of the model, we compare the experimental results to the outputs of both the original model [6], which does not take into account laser defocusing and multiple reflections and the developed model described in Section 2. This comparison is presented in Table 3 and depicted in Fig. 12.

As expected, the enthalpy method-based model without defocusing provisions overestimates the achieved cutting depth and underestimates the achieved kerf, especially for large sheet thickness. The model developed in this work provides a much better approximation. Especially, as long as the achieved cutting depth is concerned, the convergence to the experimental results is very satisfactory at the range of 10–15%.

3.3 Heat-affected zone

The developed simulation tool provides the temperature field in the workpiece. Therefore, it is possible to study the heat-affected zone (HAZ) by the laser cutting process. This study is used as a supplemental validation of the model. According to an analysis of the heat-affected zone generated by CO₂ laser, while cutting of low carbon steel made by M. Zaied et al. [43], the HAZ width of the S235 steel is an increasing, almost linear function of the laser power. In this work, HAZ is defined as the region of the workpiece that has been heated over 700 K. The HAZ predicted by the simulation tool can be easily derived from the temperature field output. Indicative examples of the temperature field for various values of the laser power are depicted in Fig. 13. The width of the HAZ at

Table 3 Cutting depth and kerf width from experiments and the enthalpy-method simulation tool without and with provisions for laser defocusing and multiple reflections in the case study of laser cutting with a CO₂ and a fiber laser source

Sheet thickness (mm)	CO ₂ laser source						Fiber laser source					
	Depth (mm)		Kerf (mm)		Depth (mm)		Kerf (mm)		Depth (mm)		Kerf (mm)	
	Experiment	Simulation w/o* with defocusing	Experiment	Simulation w/o with defocusing	Experiment	Simulation w/o with defocusing	Experiment	Simulation w/o with defocusing	Experiment	Simulation w/o with defocusing	Experiment	Simulation w/o with defocusing
4.0	4.0	2.7 2.8	0.4	0.47 0.59	4.0	4.4 4.0	0.25	0.21 0.37				
6.0	6.0	6.2 4.5	0.6	0.51 0.71	6.0	8.0 8.0	0.55	0.35 0.55				
8.0	8.0	7.9 7.3	0.8	0.61 0.75	8.0	16.0 9.5	0.6	0.37 0.65				
10.0	10.0	12.0 9.3	0.9	0.61 0.90	10.0	20.0 10.0	0.9	0.48 0.73				

*w/o stands for without

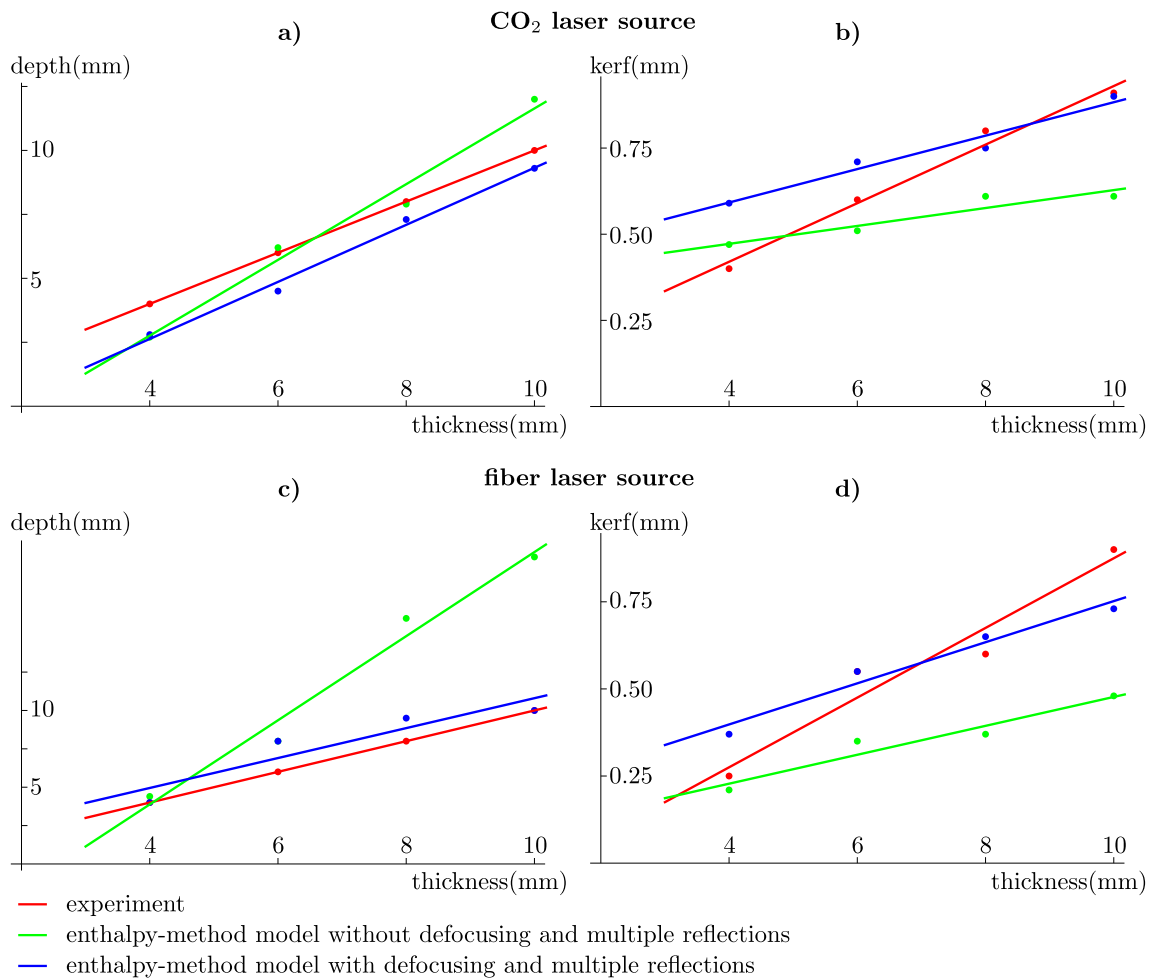


Fig. 12 Comparison of cutting depth (a and c) and kerf (b and d) for a CO₂ (a and b) and a fiber (c and d) laser source, between experiments and model output

the horizontal plane as predicted by the simulation tool for various values of the laser power is presented in Table 4 and depicted in Fig. 14.

The model outputs show that the HAZ increases as the laser power increases, in line with the literature results [43]. This is also clearly visible in the indicative examples of the temperature field that are depicted in Fig. 13. These examples show that the HAZ width is an increasing function of laser power at both the horizontal and vertical planes.

3.4 Dependence of keyhole on the focal plane

An issue that is closely related to the effect of the defocusing is the dependence of the achieved keyhole depth on the position of the focal plane. When the focal plane lies above the workpiece surface, the in-falling laser beam intensity reaching the workpiece surface is smaller than the intensity that falls on the workpiece when the focal plane lies at the workpiece surface, therefore resulting in a smaller keyhole depth.

The same holds if the focal plane lies very deeply inside the workpiece. In the latter case, the laser may never manage to produce a keyhole as deep as the position of the focal plane. Obviously, there is an optimum depth for the focal plane and several studies support that this lies at about one-third of the depth of the workpiece [14, 15].

Using the developed simulation tool, we performed an investigation of this issue for two different values of sheet thickness: $w = 4$ mm and $w = 6$ mm with a fiber laser source. In both cases, the laser power and speed were selected as optimal values from the literature, i.e., as values that when the focal plane lies at the appropriate location successful cutting of the laminate is achieved. Then, only the position of the focal plane was varied in the simulations. The results are presented in Table 5 and depicted in Fig. 15.

As visible in both Table 5 and Fig. 15, the maximal cutting depth is achieved when the focal plane lies at about one-third of the sheet thickness below the top surface, i.e., when $\frac{df}{w} \simeq \frac{1}{3}$, in line with the literature. Furthermore, this maximal cutting depth is approximately equal to the sheet thickness in

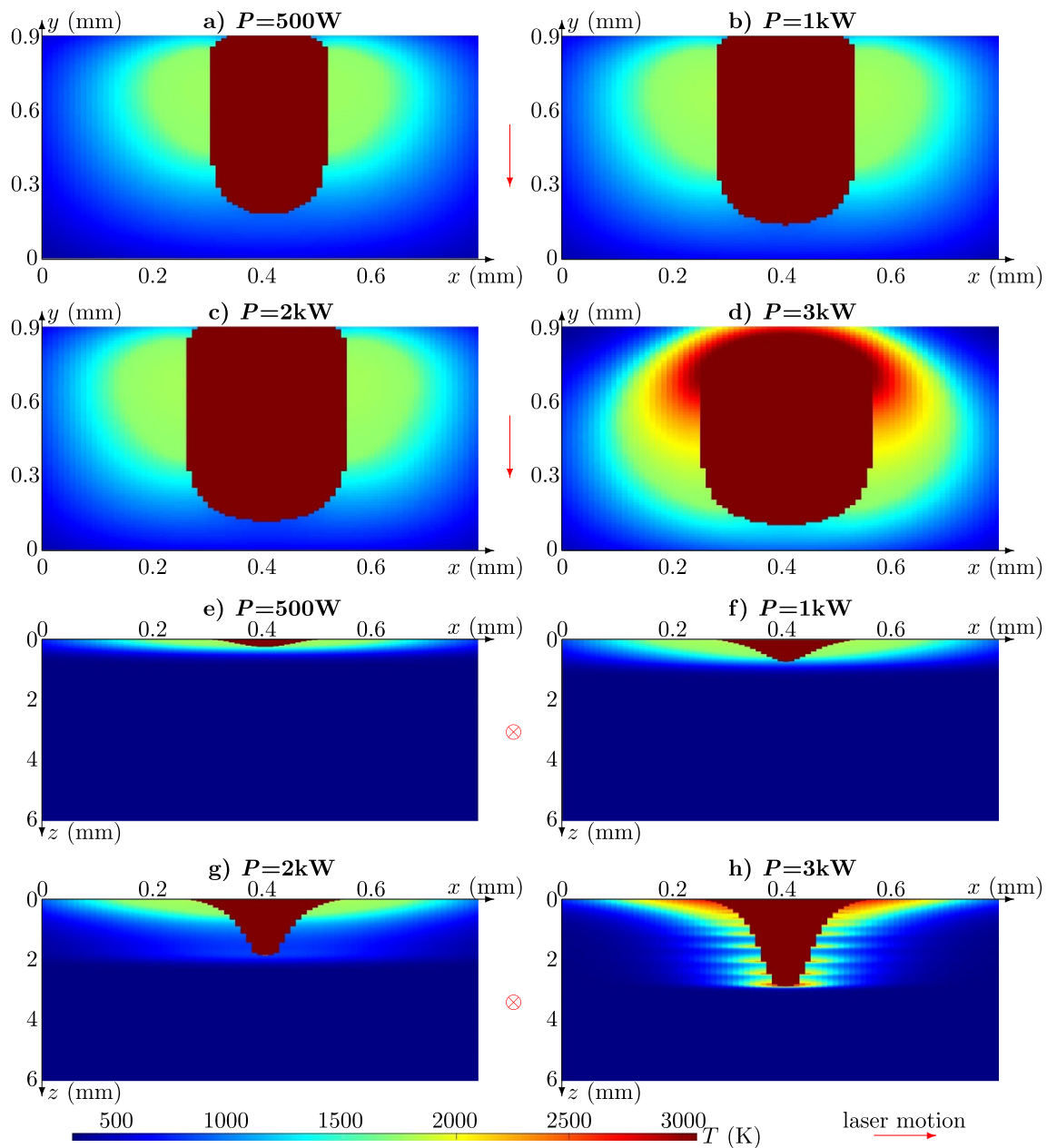


Fig. 13 The temperature field in the horizontal plane at the top surface of the substrate (**a**, **b**, **c**, and **d**) and the vertical plane that is perpendicular to the laser beam motion (**e**, **f**, **g**, and **h**) for various values of the laser power

both cases. The reader should bear in mind that the simulated workpiece width was 10% larger than the actual laminate width in order to better capture the process performance. The above provides an additional validation of the developed model.

3.5 Running times

The structure of the model that has been presented in Section 2 favors parallel computing; it can be easily applied at the computational loops that calculate the heat currents and

temperature field at each lattice cell. These loops can be distributed to many cores of the CPU, essentially assigning a part of the lattice at each core, improving the computational time. However, in this work, the code has not been parallelized and it only leverages process-modelling techniques so that it is fast enough for engineering decisions at early design phases.

The computational efficiency of the proposed method is proven by the fact that the simulation requires approximately 120 min for the case of minimum depth ($w = 4$ mm) and 6 h for the case maximum depth ($w = 10$ mm) on a typical PC

Table 4 The HAZ width on the horizontal plane as a function of the laser power according to the model

Laser power (kW)	HAZ width (mm)
0.5	0.67
1.0	0.73
1.5	0.75
2.0	0.80
3.0	1.00

(Intel Core I7-7820X CPU @ 3.60 GHz, 64 GB of RAM). Indicatively, the domain size was 0.8 mm × 0.8 mm × (1.5 × sheet thickness) with a cell size of 10 μm × 10 μm × 16 μm. The transient simulation was running for a simulation time of 5 ms with a time step of 1 μsec. The proposed model provides a significantly lower computational time than the more traditional methods in the literature, e.g., [44].

4 Discussion

The validation of the model pointed out the low computational time and the accordance of results with real-life experiments. The model has been tested in the laser cutting process with inert assisting gas.

The model can be used in an attempt to reduce the energy footprint of the laser cutting process, since the energy efficiency of the process can be calculated for various combinations of materials and process parameters. An appropriate definition of the energy efficiency in the laser cutting process [45] can easily be incorporated into the model in order to study the dependence of the efficiency of the process on process parameters such as power, speed, laser wavelength, or the focal level. The material properties are also a significant parameter to be considered during the examination of process efficiency, since more reflective materials such as copper could ask for higher levels of power. Therefore, vari-

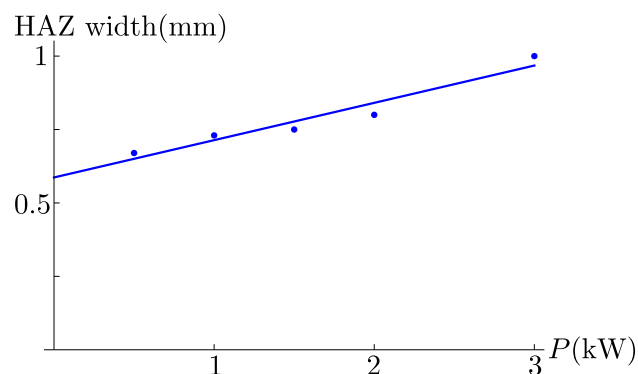


Fig. 14 The HAZ width on the horizontal plane as a function of the laser power according to the model

Table 5 The achieved cut depth as a function of the position of the focal plane relative to the workpiece surface

	Case study 1	Case study 2
Sheet width	$w = 4 \text{ mm}$	$w = 6 \text{ mm}$
Laser power	$P = 3 \text{ kW}$	$P = 3 \text{ kW}$
Spot radius	$r_0 = 85 \text{ }\mu\text{m}$	$r_0 = 85 \text{ }\mu\text{m}$
Focal length	$f = 190 \text{ mm}$	$r_0 = 190 \text{ mm}$
Laser speed	$v = 83 \text{ mm/s}$	$v = 30 \text{ mm/s}$
$\frac{df}{w}$	Cutting depth (mm)	
0	3.6	5.2
1/6	3.8	6.2
1/3	4.0	6.6
1/2	3.8	6.2
2/3	3.4	4.6

ous sources of lasers should be examined for each case since the reflectivity of the material has a strong dependence on the wavelength. This information can be introduced to the model to create a map for the dependence of process energy efficiency on the process variables.

The same workflow can be followed for the keyhole laser welding, since the process principles are the same and the model can be used without modifications. Only the KPIs that characterize the quality and the energy efficiency of the process should be adapted accordingly. Once again, the process efficiency can be examined in the same way as in the case of laser cutting, defining the efficient process window via the mapping of the effect of process variables on the process efficiency.

Finally, the examination of HAZ and the thermal history of the workpiece could be used in order to link the process parameters with the residual stresses in keyhole laser welding. This output is of interest for the user since it is

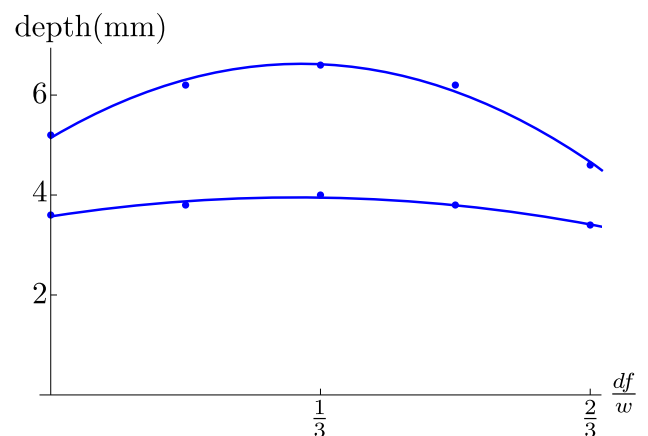


Fig. 15 The achieved cut depth as a function of the position of the focal plane relative to the workpiece surface

known that on the heat-affected zone, the material properties are downgraded and heat treatments are usually proposed. Via the direct calculation of the temperature field by the model, strategies to reduce residual stresses could be developed in order to improve the quality of the workpiece. The experimental validation of these features would require the experimental specification of the heat map during the laser welding process in real time.

5 Conclusions

The inclusion of laser beam defocusing and the alteration of the effective reflectivity of the keyhole to the enthalpy-method-based finite-differences algorithm significantly improves the convergence of the model predictions with the experimental data in keyhole laser processes, such as laser cutting, without adding significantly to the computational complexity. The improvement is quantified via the comparison of the experimental cutting depth and kerf dimension to those predicted by the model, as well as via the investigation of the dependency of the HAZ on laser power and the sensitivity of the cutting depth on the position of the focal plane. Moreover, the computational times for an industrial case study with SS304 as working material and CO₂ and fiber laser machines as laser sources are almost half of those in the literature, while the accuracy of the model is comparable to the accuracy of multi-physics models. Apart from the quality of the model predictions, the model can be easily used for different materials or laser sources by adjusting the material and laser parameters. As future work, the tool can be used for the study of the energy efficiency of laser cutting and keyhole laser welding. An important additional advantage of the model is the fact it provides the full thermal history of the workpiece as a direct output, and thus, it can be used to study the HAZ and calculate the residual stresses in the case of the laser welding process.

Author contribution Not applicable

Funding This work was partially supported by the European Union's Horizon Europe research and innovation program DaCapo (Grant agreement No 101091780).

Data availability Not applicable

Code and materials availability Not available

Declarations

Ethics approval Not applicable

Consent to participate Not applicable

Consent for publication Not applicable

Conflict of interest The authors declare no competing interests.

Open Access This article is licensed under a Creative Commons Attribution 4.0 International License, which permits use, sharing, adaptation, distribution and reproduction in any medium or format, as long as you give appropriate credit to the original author(s) and the source, provide a link to the Creative Commons licence, and indicate if changes were made. The images or other third party material in this article are included in the article's Creative Commons licence, unless indicated otherwise in a credit line to the material. If material is not included in the article's Creative Commons licence and your intended use is not permitted by statutory regulation or exceeds the permitted use, you will need to obtain permission directly from the copyright holder. To view a copy of this licence, visit <http://creativecommons.org/licenses/by/4.0/>.

References

- Molian PA (1993) Dual-beam CO₂ laser cutting of thick metallic materials. *J Mater Sci* 28(7):1738–1748. <https://doi.org/10.1007/bf00595740>
- Panagiotopoulou VC, Papacharalampopoulos A, Stavropoulos P (2023) Developing a manufacturing process level framework for green strategies KPIs handling. In: Kohl H, Seliger G, Dietrich F (eds) *Manufacturing Driving Circular Economy*. Springer, Cham, pp 1008–1015
- Stavropoulos P, Panagiotopoulou VC (2022) Carbon footprint of manufacturing processes: conventional vs. non-conventional. *Processes* 10:1858. <https://doi.org/10.3390/pr10091858>
- Quintino L, Assunção E (2013) Chapter 6 - conduction laser welding. In: Katayama S (ed.) *Handbook of laser welding technologies*, Woodhead Publishing, Sawston, UK, pp 139–162. <https://doi.org/10.1533/9780857098771.1.139>
- Troy RA, Simonds BJ, Tanner JR, Fraser JM (2020) Simultaneous in operando monitoring of keyhole depth and absorptance in laser processing of AISI 316 stainless steel at 200 kHz. *Procedia CIRP* 94:419–424. <https://doi.org/10.1016/j.procir.2020.09.157>
- Stavropoulos P, Pastras G, Souflas T, Tzimanis K, Bikas H (2022) A computationally efficient multi-scale thermal modelling approach for PBF-LB/M based on the enthalpy method. *Metals* 12(11):1853. <https://doi.org/10.3390/met12111853>
- Pastras G, Fysikopoulos A, Stavropoulos P, Chryssolouris G (2014) An approach to modelling evaporation pulsed laser drilling and its energy efficiency. *Int J Adv Manufac Technol* 72:1227–1241. <https://doi.org/10.1007/s00170-014-5668-z>
- Pastras G, Fysikopoulos A, Giannoulis C, Chryssolouris G (2014) A numerical approach to modeling keyhole laser welding. *Int J Adv Manufac Technol* 78:723–736. <https://doi.org/10.1007/s00170-014-6674-x>
- Kim K, Lee J, Cho H (2010) Analysis of pulsed Nd:YAG laser welding of AISI 304 steel. *J Mech Sci Technol* 24:2253–2259. <https://doi.org/10.1007/s12206-010-0902-6>
- Duley E, Biro Y, Zhou N (2021) Numerical modelling and experimental validation of the effect of laser beam defocusing on process optimization during fiber laser welding of automotive press-hardened steels. *J Manufac Processes* 67:535–544. <https://doi.org/10.1016/j.jmapro.2021.05.006>

11. Papacharalampopoulos A, Stavropoulos P (2023) Manufacturing process optimization via digital twins: definitions and limitations. In: Kim KY, Monplaisir L, Rickli J (eds.) *Flexible Automation and Intelligent Manufacturing: The Human-Data-Technology Nexus*, Springer, Cham, pp 342–350. https://doi.org/10.1007/978-3-031-18326-3_33
12. Stavropoulos P (2022) Digitization of manufacturing processes: from sensing to twinning. *Technologies* 10:98. <https://doi.org/10.3390/technologies10050098>
13. Courtois M, Carin M, Le Masson P, Gaied S, Balabane M (2014) A complete model of keyhole and melt pool dynamics to analyze instabilities and collapse during laser welding. *J Laser Appl* 26(4):042001. <https://doi.org/10.2351/1.4886835>
14. Pang S, Chen X, Li W, Shao X, Gong S (2016) Efficient multiple time scale method for modeling compressible vapor plume dynamics inside transient keyhole during fiber laser welding. *Optics Laser Technol* 77:203–214. <https://doi.org/10.1016/j.optlastec.2015.09.024>
15. Mei H, Xiao R, Zuo T (1996) Theoretical study on the influence of defocusing on penetration in keyhole laser welding. In: Deng SS, Wang SC (eds.) *Laser processing of materials and industrial applications*. Society of Photo-Optical Instrumentation Engineers (SPIE) Conference Series, vol. 2888, pp 346–351. <https://doi.org/10.1117/12.253144>
16. Stelzer S, Mahrle A, Wetzig A, Beyer E (2013) Experimental investigations on fusion cutting stainless steel with fiber and CO₂ laser beams. *Physics Procedia* 41:399–404. <https://doi.org/10.1016/j.phpro.2013.03.093>
17. Tenner F, Brock C, Klämpfl F, Schmidt M (2015) Analysis of the correlation between plasma plume and keyhole behavior in laser metal welding for the modeling of the keyhole geometry. *Optics Lasers Eng* 64:32–41. <https://doi.org/10.1016/j.optlaseng.2014.07.009>
18. Dilger P, Eschner E, Schmidt M (2020) Camera-based closed-loop control for beam positioning during deep penetration welding by means of keyhole front morphology. *Procedia CIRP* 94:758–762. <https://doi.org/10.1016/j.procir.2020.09.140>
19. Fabbro R (2020) Depth dependence and keyhole stability at threshold, for different laser welding regimes. *Appl Sci* 10:1487. <https://doi.org/10.3390/app10041487>
20. Medale M, Touvrey C, Fabbro R (2020) An axi-symmetric thermo-hydraulic model to better understand spot laser welding. *European J Comput Mech* 17:795–806. <https://doi.org/10.3166/remn.17.795-806>
21. Shehryar M, Khan M, Razmpoosh H, Macwan A, Biro E, Zhou Y (2021) Optimizing weld morphology and mechanical properties of laser welded Al-Si coated 22mnb5 by surface application of colloidal graphite. *J Mater Process Technol* 293. <https://doi.org/10.1016/j.jmatprotec.2021.117093>
22. Razmpoosh MH, Shehryar Khan M, Ghatei Kalashami A, Macwan A, Biro E, Y. Z. (2021) Effects of laser beam defocusing on high-strain-rate tensile behavior of press-hardened Zn-coated 22MnB5 steel welds. *Optics Laser Technol* 141. <https://doi.org/10.1016/j.optlastec.2021.107116>
23. Rahman-Chukkan J, Vasudevan M, Muthukumaran S, Ravi-Kumar R, Chandrasekhar N (2015) Simulation of laser butt welding of AISI 316L stainless steel sheet using various heat sources and experimental validation. *J Mater Process Technol* 219:48–59. <https://doi.org/10.1016/j.jmatprotec.2014.12.008>
24. Martinson P, Daneshpour S, Kocak M, Riekehr S, Staron P (2009) Residual stress analysis of laser spot welding of steel sheets. *Mater Design* 30:3351–3359. <https://doi.org/10.1016/j.matdes.2009.03.041>
25. Wu CS, Wang HG, Zhang YM (2006) A new heat source model for keyhole plasma arc welding in fem analysis of the temperature profile. *Welding J* 85(12):284
26. Metelkova J, Kinds Y, Kempen K, Formanoir C, Witvrouw A, Hooreweder BV (2018) On the influence of laser defocusing in selective laser melting of 316L. *Additive Manufac* 23:161–169. <https://doi.org/10.1016/j.addma.2018.08.006>
27. Yaasin AM, Morgan D, Patrice P, Michel B, Remy F (2023) Physical mechanisms of conduction-to-keyhole transition in laser welding and additive manufacturing processes. *Optics Laser Technol* 158(Part A):108811. <https://doi.org/10.1016/j.optlastec.2022.108811>
28. Riveiro A, Quintero F, Boutinguiza M, Val JD, Comesaña R, Lusquiños F, Pou J (2019) Laser cutting: a review on the influence of assist gas. *Materials* 12(1):157. <https://doi.org/10.3390/ma12010157>
29. Olsen FO, Alting L (1989) Cutting front formation in laser cutting. *CIRP Annals* 38:215–218. [https://doi.org/10.1016/s0007-8506\(07\)62688-2](https://doi.org/10.1016/s0007-8506(07)62688-2)
30. Fieret J, Terry MJ, Ward BA (1986) Aerodynamic interactions during laser cutting. In: Duley WW, Weeks RW (eds.) *Laser processing: fundamentals, applications, and systems engineering*, vol. 0668, pp 53–62. SPIE, 0668. <https://doi.org/10.1117/12.938884>
31. Olsen F (2006) An evaluation of the cutting potential of different types of high power lasers. Paper presented at 25th International Congress on Laser Materials Processing and Laser Microfabrication, Wuhan, People's Republic of China, 23–25 March 2010. <https://doi.org/10.2351/1.5060824>
32. Yilbas BS (2001) Effect of process parameters on the kerf width during the laser cutting process. *Proceedings of the Institution of Mechanical Engineers, Part B: Journal of Engineering Manufacture* 215(10):1357–1365. <https://doi.org/10.1243/0954405011519132>
33. Vicanek M, Simon G (1987) Momentum and heat transfer of an inert gas jet to the melt in laser cutting. *J Phys D: Appl Phys* 20(9):1191–1196. <https://doi.org/10.1088/0022-3727/20/9/016>
34. Khoshaim A, Elsheikh A, Moustafa E, Basha M, Showaib E (2021) Experimental investigation on laser cutting of PMMA sheets: effects of process factors on kerf characteristics. *J Mater Res Technol* 11:235–246. <https://doi.org/10.1016/j.jmrt.2021.01.012>
35. Miyagi M, Wang J (2020) Keyhole dynamics and morphology visualized by in-situ X-ray imaging in laser melting of austenitic stainless steel. *J Mater Process Technol* 282. <https://doi.org/10.1016/j.jmatprotec.2020.116673>
36. Sharp MC (2015) 4 - laser processing of medical devices. In: Meglinski I (ed) *Biophotonics for medical applications*. Woodhead Publishing Series in Biomaterials, Woodhead Publishing, pp 79–98. 9780857096623 10.1016/B978-0-85709-662-3.00004-X
37. Isamu M, Cvecek K, Schmidt M (2020) Advances of laser welding technology of glass -science and technology-. *J Laser Micro/Nanoeng* 15(2). <https://doi.org/10.2961/jlmn.2020.02.1001>
38. Slătineanu L, Coteață M, Dodun O, Beșliu I (2013) Obtaining slots and channels by using a 1070nm wavelength laser. *Procedia CIRP* 6:479–485. <https://doi.org/10.1016/j.procir.2013.03.042>
39. Zhang H, Xia H, Fan M, Zheng J, Li J, Tian X, Zhou D, Huang Z, Zhang F, Zhang R (2023) Observation of wavelength tuning in a mode-locked figure-9 fiber laser. *Photonics* 10:184. <https://doi.org/10.3390/photonics10020184>
40. Perez-Herrera RA, Lopez-Amo M (2013) Multi-wavelength fiber lasers. In: Harun SW, Arof H (eds.) *Current Developments in Optical Fiber Technology*. IntechOpen, Rijeka. Chap. 17. <https://doi.org/10.5772/53398>
41. Valencia JJ, Queded PN (2008) Thermophysical properties. In: Viswanathan S, Apelian D, Donahue RJ, DasGupta B, Gywn M, Jorstad JL, Monroe RW, Sahoo M, Prucha TE, Twarog D (eds.) *Casting*. ASM Handbook, vol. 15, pp 468–481. ASM International, Materials Park, OH, USA. <https://doi.org/10.31399/asm.hb.v15.a0005240>
42. Xie J, Kar A (1999) Laser welding of thin sheet steel with surface oxidation. *Welding J* 78(10):343–348

43. Zaied M, Miraoui I, Boujelbene M, Bayraktar E (2013) Analysis of heat affected zone obtained by CO₂ laser cutting of low carbon steel (s235). AIP Conference Proceedings 1569(1):323–326. <https://doi.org/10.1063/1.4849285>
44. Markus SG (2006) On gas dynamic effects in the modelling of laser cutting processes. Appl Math Modell 30(4):307–318. <https://doi.org/10.1016/j.apm.2005.03.021>
45. Fysikopoulos A, Pastras G, Alexopoulos T, Chryssolouris G (2014) On a generalized approach to manufacturing energy efficiency. Int J Adv Manufac Technol 73:1437–1452. <https://doi.org/10.1007/s00170-014-5818-3>

Publisher's Note Springer Nature remains neutral with regard to jurisdictional claims in published maps and institutional affiliations.